



## Postmortem analysis of calendar-aged graphite/LiFePO<sub>4</sub> cells

M. Kassem\*, C. Delacourt

Laboratoire de Réactivité et Chimie des Solides, UMR CNRS 7314, Université de Picardie Jules Verne, 80039 Amiens, France

### HIGHLIGHTS

- Postmortem results of calendar-aged commercial graphite/LFP cells.
- Capacity loss is directly related to the severity of storage conditions (temperature and SOC).
- Electrodes develop rich surface chemistry upon storage.
- Loss of cyclable lithium is the main source of aging.
- Results suggest the absence of active material losses at both positive and negative electrodes.

### ARTICLE INFO

#### Article history:

Received 1 September 2012

Received in revised form

6 December 2012

Accepted 21 January 2013

Available online 13 February 2013

#### Keywords:

Graphite/LFP cells

Storage

Postmortem analysis

Electrochemical tests

Active materials characterization

### ABSTRACT

A series of graphite/LFP commercial cells, stored under 3 different conditions of temperature (30, 45, and 60 °C) and SOC (30, 65, and 100%) during up to 8 months, are disassembled and analyzed in order to identify aging phenomena. The recovered positive and negative electrodes are studied using X-ray diffraction, scanning electron microscopy, Fourier transform infrared spectroscopy, and electrochemical testing. The maximum lithium stoichiometry in the recovered cathodes, derived both from XRD data and from electrochemical titration, decreases with an increase of storage temperature and storage SOC. This result confirms that the capacity fade of the commercial cells is caused by the loss of cyclable lithium. From capacity measurements on individual electrodes, any loss of active material is ruled out. Cyclable lithium loss arises from the growth of the solid electrolyte interphase at the anode, as outlined by the presence of a thick and fluffy film at the graphite particle surface for severe aging conditions (e.g., T = 60 °C and SOC = 100%) and an increase of the impedance. Evidence for side reactions at the LFP electrode is provided as well, as demonstrated by the presence of F-rich particles and an impedance increase for the electrodes that aged the most.

© 2013 Elsevier B.V. All rights reserved.

## 1. Introduction

Lithium-ion batteries, first commercialized by Sony Energy Tech. [1], are nowadays the dominant rechargeable systems on the market. Their high energy and power densities favor their utilization as power sources in a wide range of applications ranging from portable electronics (e.g., cellular phones, digital cameras, and laptop computers) to electric transportation [e.g., electric vehicles (EVs) and hybrid electric vehicles (HEVs)]. Lithium-ion batteries vary in performance depending on the electrode active materials they are based on. Cells with different cathode materials can be

found on the market, such as those based on layered oxides, spinel oxides, and transition metal phosphates [LiFePO<sub>4</sub> (LFP)].

The olivine LFP cathode, generally described as thermally stable and low toxic, has a theoretical capacity of 170 mAh g<sup>-1</sup> [2,3]. The LFP-based cells are considered as promising candidates for application in high-rate devices (e.g., HEV); however, just like other battery systems, they suffer capacity and power fade during both cycling and storage. Thus, aging of these batteries remains one of biggest concerns of automakers and final users, since it can directly impact the terms of warranty as well as the cost. Several aging studies of the long-term cycling performance of LFP-based cells are found in the literature [4–16]. The main results of these papers are summarized in our previous manuscript [17]. More generally, the performance loss of aged cells can be attributed to several processes such as (i) the loss of cyclable lithium (otherwise called primary loss), which is related to side reactions occurring at both

\* Corresponding author. Tel.: +33 3 22 82 75 89; fax: +33 3 22 82 75 90.

E-mail addresses: [mohammad.kassem@u-picardie.fr](mailto:mohammad.kassem@u-picardie.fr) (M. Kassem), [charles.delacourt@u-picardie.fr](mailto:charles.delacourt@u-picardie.fr) (C. Delacourt).

electrodes [e.g., solid electrolyte interphase (SEI) growth at the carbonaceous anode due to electrolyte decomposition] and leading to an increase of the cell imbalance, (ii) the loss of active materials (otherwise called secondary loss) and arising from, e.g., material dissolution, structural degradation, particle isolation, and electrode delamination, and (iii) impedance increase of the cell (e.g., because of passive films at the active particle surface and loss of electrical contact within the porous electrode). Meanwhile, studies dedicated to calendar aging (i.e., aging under storage) of LFP-based cells are scarce [15–17], though calendar aging is of major relevance in the evaluation of cell degradation, considering that a personal EV spends about 95% of its time in parking mode.

Recently, we have investigated the storage effect on the performance of commercial graphite/LFP cells [17]. The capacity fade of cells was studied and the effect of temperature and state of charge (SOC) was analyzed. It was found that, after storage, all the cells except those stored at 30 °C exhibit capacity fade. The extent of capacity fade strongly increases with storage temperature and to a lesser extent with the SOC. From an in-depth nonintrusive data analysis, cyclable lithium loss was identified as the main source of capacity fade. This loss mostly arises from side reactions taking place at the anode, e.g., solvent decomposition leading to the SEI growth. However, the existence of reversible capacity loss also suggested the presence of side reactions occurring at the cathode, which are less prominent than those at the anode. The analyses did not show any evidence of active material loss in any electrode. Furthermore, the cells suffered only moderate change in internal resistance. According to an electrochemical impedance spectroscopy (EIS) analysis, the overall impedance increase was 70% or less, which barely affects the rate capability of the cells even at a 5 C rate.

In this paper, the cells studied in Ref. [17] are dismantled and postmortem analyses are performed. The goals are (i) to confirm the results derived from the nonintrusive analyses of the cells and (ii) to get some more understanding of the underlying aging phenomena. The structure and surface morphology of both electrodes harvested from dismantled cells before and after storage are investigated by X-ray diffraction (XRD) and scanning electron microscopy (SEM), respectively. Fourier transform infrared spectrometry (FTIR) is used to identify species in the electrodes that result from aging phenomena. Electrochemical tests on LFP and graphite electrodes are also conducted.

## 2. Experimental

Experimental studies were performed on graphite/LiFePO<sub>4</sub> cells (LiFeBatt™ X1P, 8 Ah, 38123 cell [18]) designed for power-type applications. These cells are based on a C–LiFePO<sub>4</sub> cathode and a graphite anode and have a nominal capacity of 8 Ah, dimensions of 123 mm long and 38 mm diameter, and weight of 290 g. The cells were stored at 3 different temperatures: 30, 45, and 60 °C, and at 3 different states of charge (SOC<sub>nom</sub>): 30, 65, and 100%. This means that there is a total of 9 different storage conditions. For each storage condition, 3 cells were aged. Thus, the total number of cells tested during this aging study amounts to 27. For the purpose of postmortem analysis, we have dismantled 10 cells (a fresh one and 9 aged cells). Each aged cell has its own specific storage condition [17]. The fresh and calendar-aged cells were opened at fully discharged state (the discharge procedure consists of a constant current/constant voltage (CCCV) discharge [i.e., 1C<sub>nom</sub> (8 A) down to 2 V and a potential hold at 2 V until a cutoff current |I| = C<sub>nom</sub>/20]) inside an argon-filled glove box (<1 ppm H<sub>2</sub>O, <10 ppm O<sub>2</sub>). The double-sided electrodes are 3.83 ± 0.06 m long for graphite and 3.73 ± 0.07 m long for LFP. For each electrode, a single piece (preferably sampled near the center of the jelly roll), was rinsed

with dimethyl carbonate (DMC Selectlyte, Merck) in order to extract the lithium salt and was then dried under vacuum in the antechamber for 1 h.

Electrochemical tests were done on the fresh and used electrodes harvested from the dismantled cells. For this purpose and for both electrodes, one side of the coating was rubbed off of the current collector using a cotton-based tissue soaked in 1-methyl-2-pyrolidinone. LFP and carbon disc electrodes with 12 mm diameter were then punched out and coin cells were assembled with a lithium metal foil as counter electrode and a Whatman GF/D borosilicate glass fiber as separator. LiPF<sub>6</sub> (1 mol L<sup>-1</sup>) in a 1:1 EC/DMC solution (LP30, Merck) was used as the electrolyte. The coin cells underwent a series of tests including (i) low-rate capacity measurements, (ii) electrochemical impedance spectroscopy (EIS), and (iii) rate-capability tests. All the tests were conducted at 25 °C in a climatic chamber (Binder KB53) by using a multipotentiostat (VMP3, Bio-logic, France). In the rest of the article, the electrochemical tests performed on coin cells are referred to as half-cell studies.

The Li/LFP (Li/graphite) coin cells were initially cycled in order to determine nominal capacity values of fresh LFP (graphite) electrodes (C<sub>nom</sub> is 1.414 mAh cm<sup>-2</sup> for LFP and 1.505 mAh cm<sup>-2</sup> for graphite). During the checkup procedure, residual electrode

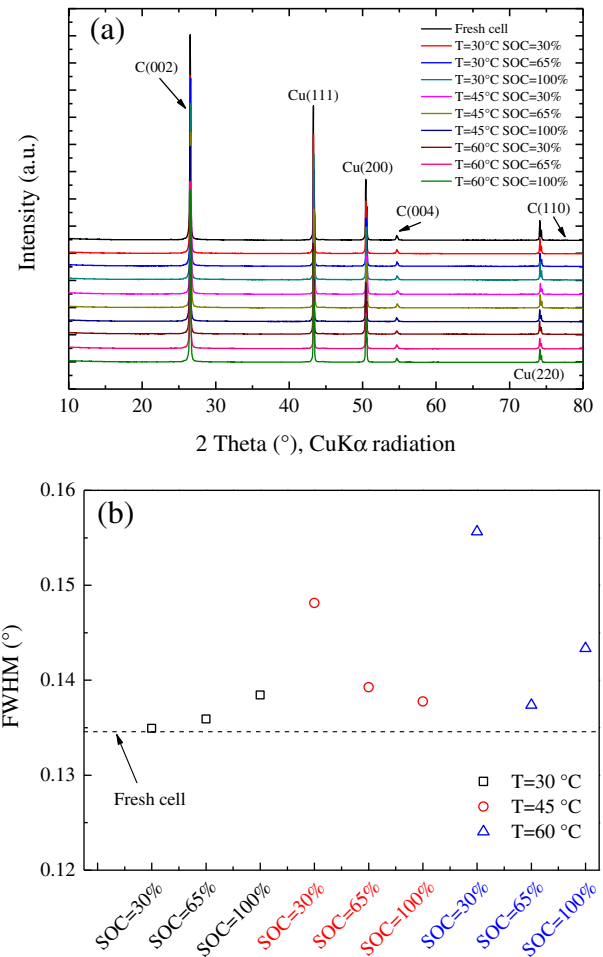


**Fig. 1.** (a) XRD patterns of the graphite electrodes recovered from the fresh cell and cells aged under different storage conditions of temperature and SOC, after they were discharged down to 2 V. (b) Full width at half maximum (FWHM) of the (002) graphite peak for all the electrodes harvested from dismantled cells.

capacities were first measured; to this end, Li/LFP coin cells were discharged (i.e., lithium insertion) to 2.0 V and the Li/graphite coin cells were charged (i.e., lithium deintercalation) to 1.5 V. A constant current/constant voltage (CCCV) protocol (CC at  $C_{\text{nom}}/10$  and CV until  $|I| < C_{\text{nom}}/50$ ), between 2.0 and 4.1 V for the LFP coin cells and between 0.0 and 1.5 V for the graphite coin cells, was used. This was followed by four charge/discharge cycles using the same CCCV protocol. Reversible “(also denoted intrinsic)” capacities consisted of the average between measured discharge (charge) capacities of the last two cycles of two LFP (graphite) coin cells. EIS measurements were carried out in the frequency range 200 kHz–10 mHz with a 5 mV RMS sinusoidal potential applied after the half-cell was left at open circuit during 1 h. The impedance spectra were measured at different nominal checkup SOCs ( $\text{SOC}_{\text{nom},\text{ck}} = 100\%, 80\%, 60\%, 40\%, 20\%, \text{ and } 0\%$ ). For the LFP coin cells, the nominal checkup SOCs were set from a fully-charged state ( $\text{SOC} = 100\%$ ) by using a  $C_{\text{nom}}/10$  discharge rate during 2, 4, 6, 8, and 10 h in order to set the  $\text{SOC}_{\text{nom},\text{ck}}$  to 80, 60, 40, 20, and 0%, respectively. For the graphite coin cells, the SOC is set from a fully discharged state. The rate-capability tests were performed by galvanostatic charge/discharge at C-rates varying between  $C_{\text{nom}}/10$  and  $5C_{\text{nom}}$ . A CCCV protocol was used for both charge and discharge modes

**Table 1**

Lattice parameters of LFP and FP phases in cathodes recovered either from a fresh cell or from cells stored at  $\text{SOC}_{\text{nom}} = 100\%$  and temperatures 45 °C or 60 °C. LFP and FP phases are both indexed in the orthorhombic Pnma space group.

Lattice parameters (Å)	Fresh	$T = 45^\circ\text{C}$ $\text{SOC}_{\text{nom}} = 100\%$	$T = 60^\circ\text{C}$ $\text{SOC}_{\text{nom}} = 100\%$
$\text{LiFePO}_4$			
$a$	10.32467 (3)	10.32621 (17)	10.32279 (12)
$b$	6.00542 (2)	6.00414 (9)	6.00424 (7)
$c$	4.69160 (2)	4.69118 (9)	4.68984 (6)
$\text{FePO}_4$			
$a$	9.82438 (11)	9.8288 (6)	9.81704 (20)
$b$	5.79535 (14)	5.7989 (4)	5.79135 (11)
$c$	4.77519 (7)	4.7734 (2)	4.77900 (9)

(CV until  $|I| < C_{\text{nom}}/50$ ), and the voltage limits specific to each individual electrode were the same as mentioned above for capacity measurements.

The structural characterization of the active materials was carried out by X-ray diffraction (XRD) using a BRUKER D4 diffractometer in the  $2\theta$  range 10–80° (Cu K $\alpha$  radiation,  $\lambda = 1.5406\text{ \AA}$ ) at ambient condition. The surface morphology of the electrodes was studied by scanning electron microscopy (SEM) using an FEI Quanta 200 microscope and elemental composition was determined using an Oxford INCA X-sight energy dispersive spectrometer (EDS). Fourier transform infrared (FTIR) spectra were measured at room temperature under air in the spectral region 4000–400  $\text{cm}^{-1}$  using the Thermo Nicolet Avatar 370 DTGS spectrometer with a resolution of 4  $\text{cm}^{-1}$ .

### 3. Results and discussion

#### 3.1. XRD measurements

In Fig. 1(a), the XRD patterns of the graphite electrodes recovered from fresh and aged cells, dismantled in their discharged state (2 V), are represented. There is no significant difference between the XRD patterns and only the peaks of copper and graphite are detected. The diffraction peaks of the stored graphite electrodes have the same angular positions as those of the fresh electrode. The

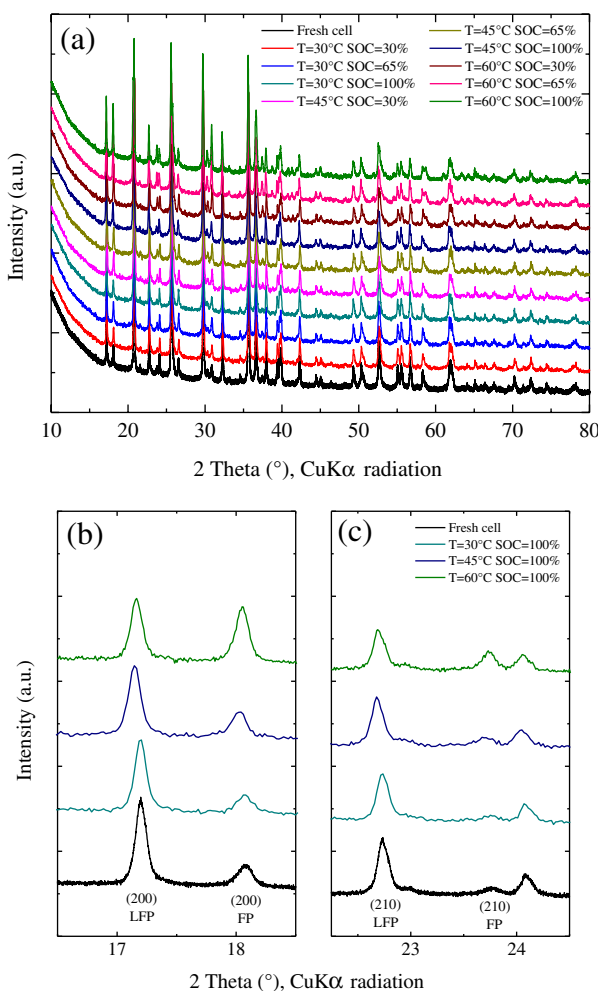


**Fig. 2.** (a) XRD patterns of the LFP electrodes recovered from the fresh cell and from cells aged under different storage conditions of temperature and SOC, after they were discharged down to 2 V. (b) and (c) show the (200) and (210) reflections of LFP and FP phases in the XRD pattern.

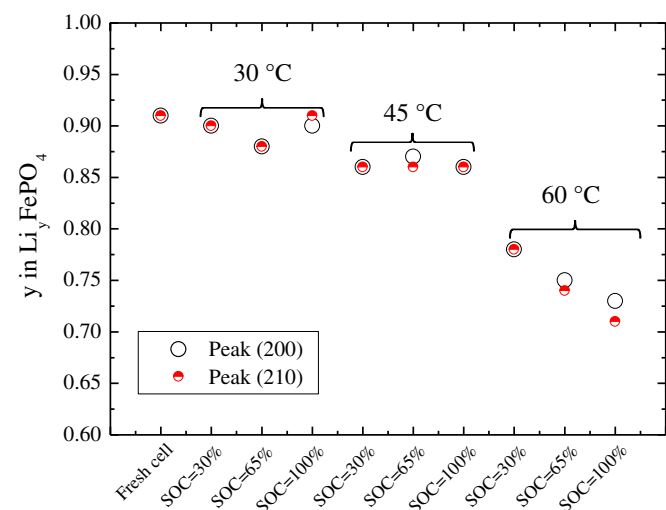


**Fig. 3.** Li stoichiometry of the cathode corresponding to the LFP/(FP + LFP) mole ratio derived from XRD patterns. Li stoichiometry is derived from both 200 (open circle) and 210 (half-open circle) reflections.

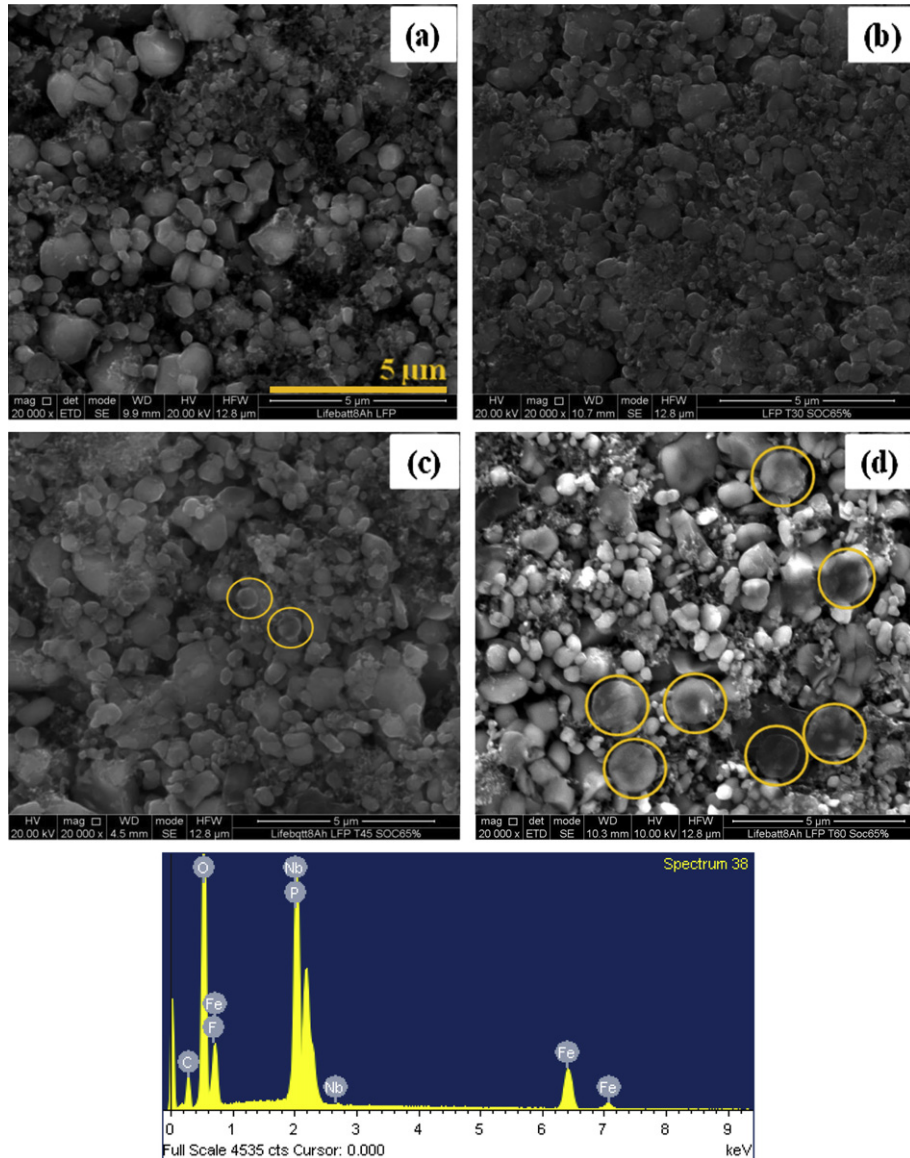


**Fig. 4.** SEM images of the LFP electrodes recovered from (a) the fresh cell and from the cells stored at  $\text{SOC}_{\text{nom}} = 65\%$  and temperatures (b)  $30^\circ\text{C}$ , (c)  $45^\circ\text{C}$ , and (d)  $60^\circ\text{C}$ . Typical EDS spectrum of some grains scattered throughout the electrode LFP surface that show the presence of Nb traces.

only difference between patterns is a slight broadening of the peaks. The full widths at half maximum (FWHM) of the (002) peak of all anode samples are represented in Fig. 1(b). In general, the FWHMs of the stored samples are slightly larger than those of the

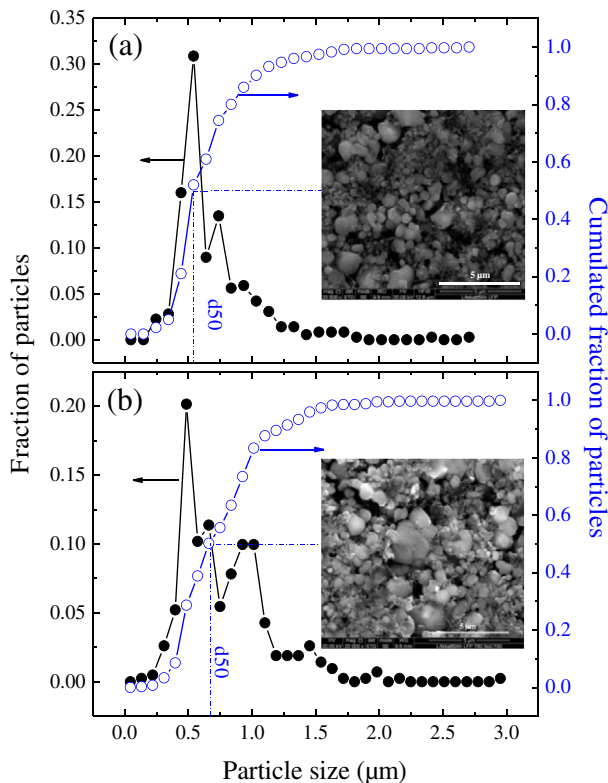
fresh one and the largest FWHM is found for the cell stored at  $60^\circ\text{C}$  and  $\text{SOC}_{\text{nom}} = 30\%$ . Such a broadening may result from a decrease in the crystallite dimension or from strains within the crystallites themselves [19].

Fig. 2(a) shows the XRD patterns of the LFP electrodes recovered from fresh and stored cells. Several phases are found, namely  $\text{LiFePO}_4$  (LFP) and  $\text{FePO}_4$  (FP), both indexed in the orthorhombic Pnma space group, graphite, and  $\text{NbOPO}_4$  as a minor compound. The full-pattern matching of a fresh sample and two stored ones ( $\text{SOC}_{\text{nom}} = 100\%$ ,  $T = 45^\circ\text{C}$  and  $60^\circ\text{C}$ ) provide us with the lattice parameters of the LFP and FP phases (Table 1). The values for the stored samples are close to those reported for the fresh one, thus indicating the absence of any structural modification of LFP and FP during calendar aging. However, the electrodes harvested from the stored cells show a decrease in the intensities of the LFP reflections accompanied by an increase of the FP reflections, as clearly seen on (200) and (210) reflections of LFP and FP phases in Fig. 2(b) and (c). The intensity ratios of the (200) or (210) peaks between LFP and FP phases were used to quantify the overall

**Table 2**

EDS results of the regular and round-shape particles found at the surface of the LFP electrodes recovered from the cells stored at  $\text{SOC}_{\text{nom}} = 65\%$  and temperatures  $45^\circ\text{C}$  and  $60^\circ\text{C}$ .

Element	Atomic%			
	Regular particles		Round-shape particles	
	45 °C	60 °C	45 °C	60 °C
Carbon	23.8	22.3	26.1	19.1
Oxygen	56.6	59.3	43.5	29.9
Fluorine	—	—	10.1	36.5
Phosphorous	10.2	9.8	9.6	7.4
Iron	9.4	8.6	10.6	6.6
Sulfur	—	—	0.1	0.5



**Fig. 5.** Particle-size distribution of LFP electrodes recovered from both fresh and aged cells, resulting from an analysis of the scanning electron micrographs displayed in insets. (a) Fresh cell and (b) cell stored at 60 °C and SOC<sub>nom</sub> = 100%.

**Table 3**

EDS results of the graphite electrodes recovered from the fresh cell and from the cells stored at SOC<sub>nom</sub> = 100% and temperatures 30, 45, and 60 °C.

Element	Atomic%			
	Fresh	30 °C	45 °C	60 °C
Carbon	83.4	91.0	89.9	86.1
Oxygen	7.3	8.4	8.9	12.3
Copper	8.5	0.1	0.3	0.2
Phosphorous	0.5	0.1	0.1	0.2
Sulfur	0.1	0.2	0.2	0.2
Fluorine	0.2	0.2	0.6	1.0

stoichiometry of the LFP electrode ( $y$  in  $\text{Li}_y\text{FePO}_4$ ), based on a calibration curve reported in Ref. [16] and built upon data from Ref. [20]. Lithium stoichiometries derived from the peak intensity are reported in Fig. 3 for all the electrodes. The fresh cell shows an initial Li stoichiometry of about 91%. The Li stoichiometry decreases to 71% for the most severe storage condition ( $T = 60$  °C and SOC = 100%). The Li stoichiometry exhibits a clear dependence on the storage temperature, whereas the effect of SOC is only visible for electrodes stored at 60 °C and is almost negligible for the other two storage temperatures.

### 3.2. Morphology of the electrodes (SEM)

SEM was used for spotting possible changes of the electrode morphology after storage. The SEM images of fresh and aged LFP electrodes are displayed in Fig. 4. The aged electrodes were recovered from the cells stored at SOC<sub>nom</sub> = 65% and temperatures 30, 45, and 60 °C. Aging leads to the appearance of round-shape

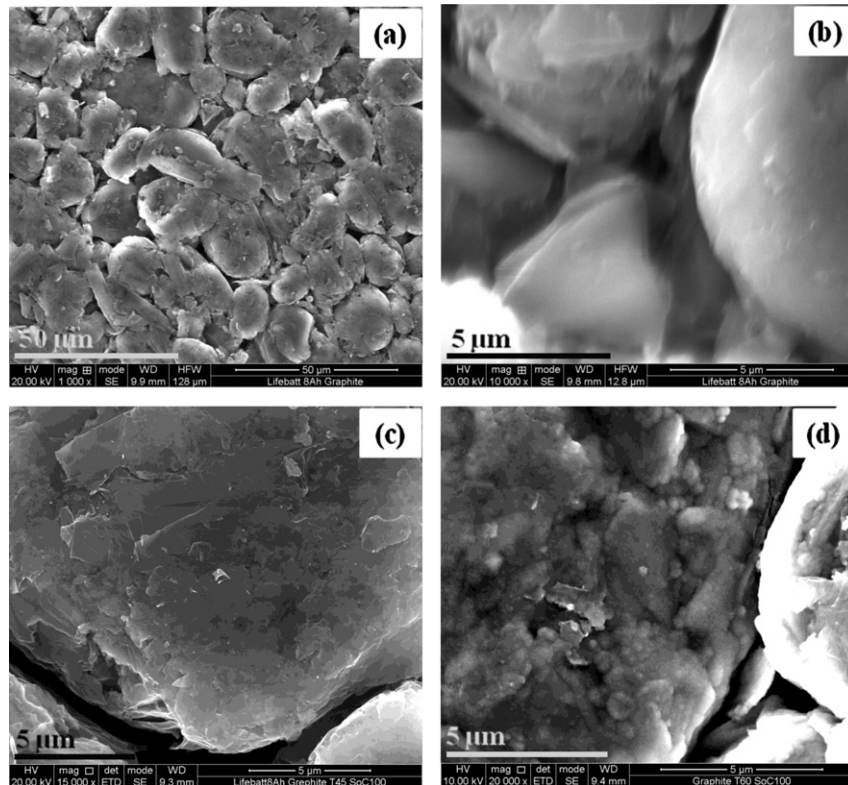


**Fig. 6.** SEM images of the graphite electrodes recovered from (a) and (b) the fresh cell and from the cells stored at SOC<sub>nom</sub> = 100% and temperatures (c) 45 °C and (d) 60 °C.

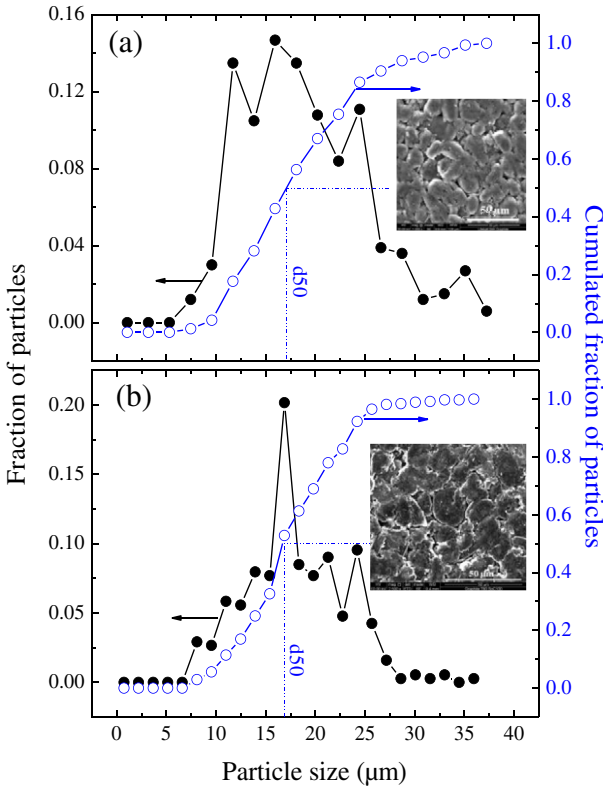


**Fig. 7.** Particle-size distribution of graphite electrodes recovered from both fresh and aged cells, resulting from an analysis of the scanning electron micrograph displayed in insets. (a) Fresh cell and (b) cell stored at 60 °C and  $\text{SOC}_{\text{nom}} = 100\%$ .

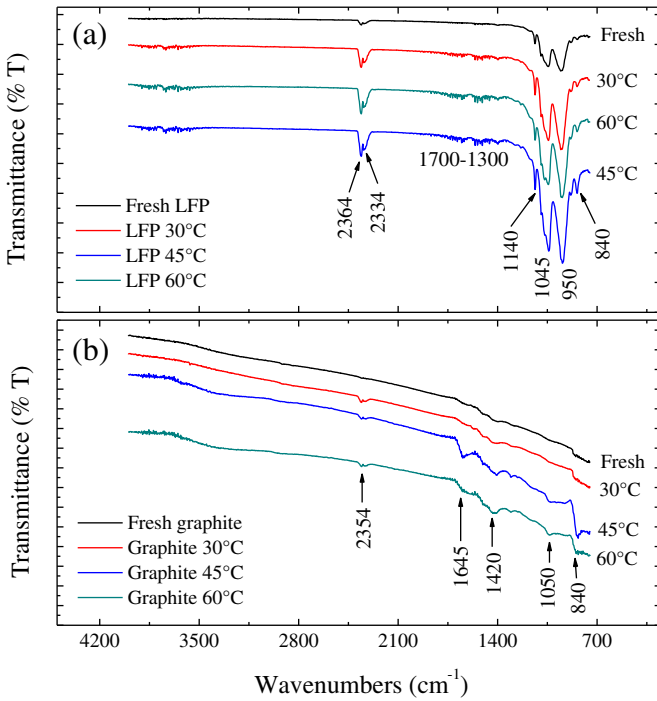


**Fig. 8.** FTIR spectra measured in reflectance mode of (a) a fresh and an aged LFP electrode and (b) a fresh and an aged graphite electrode. Both aged LFP and graphite electrodes are recovered from cells stored  $\text{SOC}_{\text{nom}} = 100\%$  and temperatures 30, 45, and 60 °C.

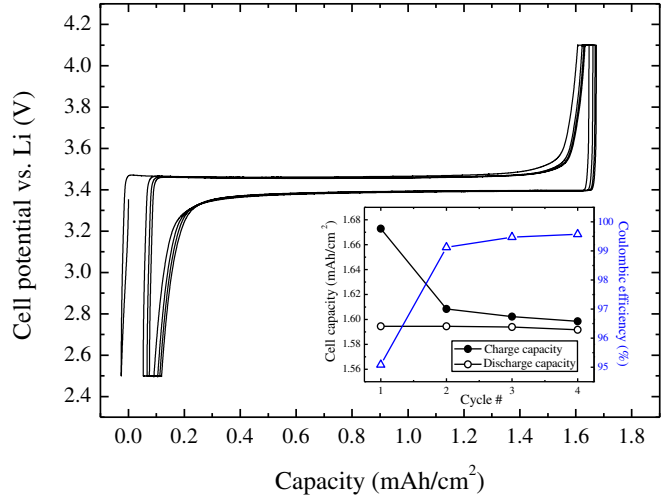


**Fig. 9.** Potential profile during the four formation cycles at 25 °C of the LFP electrode recovered from a fresh cell. Conditions: CC at  $C_{\text{nom}}/10$  and CV until  $|I| < C/50$ . Inset: charge and discharge CCCV capacities (circles) and coulombic efficiency (triangles).

particles as seen in Fig. 4(c) and (d). At the storage temperature of 45 °C, i.e., Fig. 4(c), the size of such particles is  $\sim 0.5\text{--}0.7 \mu\text{m}$ . These same particles are more abundant and increase in size ( $\sim 1.3 \mu\text{m}$ ) for the storage temperature of 60 °C (Fig. 4(d)). The EDS analyses of these round-shape particles show that they are rich in fluorine and that the atomic percentage of fluorine within these particles becomes larger with the severity of the storage condition (Table 2). The fact that the particles are smaller at 45 °C than at 60 °C might account for the lesser fraction of F, because the EDS analysis is on about  $1 \mu\text{m}^3$  volume. The lesser fraction of P, O, and Fe in the analysis on the 60 °C sample supports this hypothesis as well. Some other Nb-containing particles, scattered throughout the electrode surface (EDS spectrum of Fig. 4), are also found. This correlates well with XRD patterns which show the presence of the  $\text{NbOPO}_4$  phase. No further morphological changes were seen from SEM. The particle-size distribution (PSD), which is determined

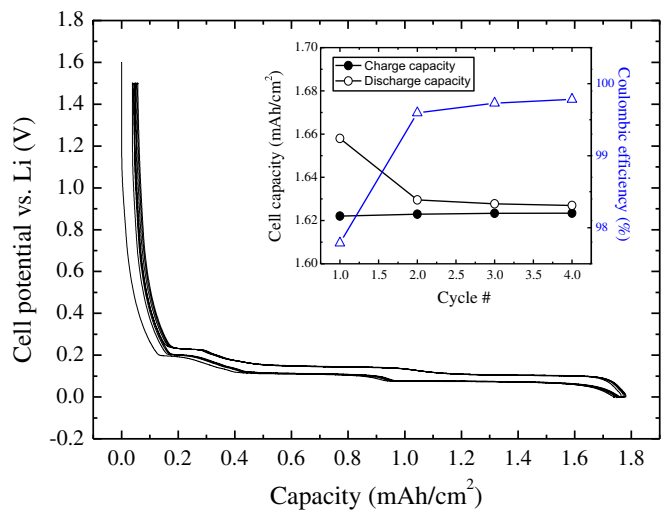


**Fig. 10.** Potential profile during the four formation cycles at 25 °C of the graphite electrode recovered from a fresh cell. Conditions: CC at  $C_{\text{nom}}/10$  and CV until  $|I| < C/50$ . Inset: charge and discharge capacities (circles) and coulombic efficiency (triangles).

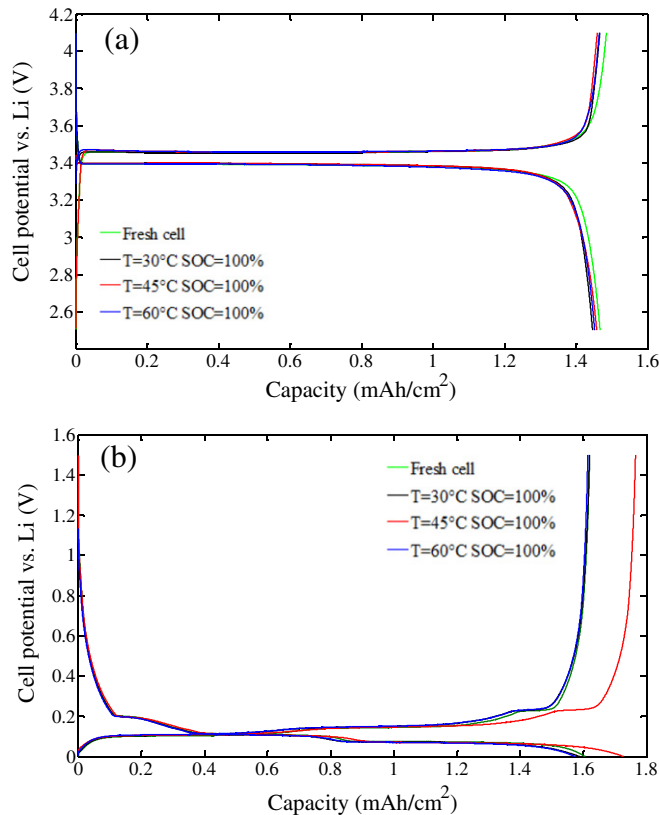


**Fig. 11.** Charge/discharge profiles of the 4th formation cycle measured at  $C_{\text{nom}}/10$  and 25 °C for both (a) LFP and (b) graphite electrodes recovered from fresh and aged cells under storage at  $\text{SOC}_{\text{nom}} = 100\%$  and different temperatures.

from the analysis of the SEM images, assuming the particles to be spherical, show that the fresh and stored electrodes are composed of grains with a size ranging from ~0.2 μm to ~2 μm. Fig. 5 presents the PSD of LFP electrodes recovered from both the fresh cell and from the cell stored at 60 °C and  $\text{SOC}_{\text{nom}} = 100\%$ . The particle size range is the same as mentioned earlier, with a  $d_{50}$  value of ~0.54 μm for the fresh LFP electrode and ~0.66 μm for the aged one. Moreover, the PSD in Fig. 5(b) looks bimodal. We do not believe that it is a result of the F-rich particles newly observed,

though, as the number of those latter particles is negligible with respect to the overall particle number used in the PSD analysis (~300–400 particles).

As for the graphite electrode, the influence of the storage conditions manifests itself by a change of the electrode color. Originally dark brown, it turns bluish for the cells aged at 60 °C. No color change was observed for the cells aged at 45 °C or less. The color of the graphite material depends on its lithium content [21], which suggests that graphite electrode aged at 60 °C are not fully delithiated even though the cell was discharged down to 2 V. Fig. 6 presents the surface morphology of graphite electrodes from disassembled fresh (a and b) and stored cells (c and d). Aging leads to some roughening of the particle facets, especially for the graphite electrode stored under the most severe conditions ( $T = 60$  °C and  $\text{SOC}_{\text{nom}} = 100\%$ ). The apparent roughness of the graphite surface is likely related to the SEI film that becomes fluffy as it grows. Table 3 shows the result of EDS analysis of the graphite electrode. The atomic percentage of oxygen in aged electrodes is relatively larger than those of the fresh electrode, which might be related with the presence of SEI compounds such as Li<sub>2</sub>CO<sub>3</sub> or lithium alkylcarbonates at the particle surface that are O-rich. In addition, no change of particle-size distribution was observed. Fig. 7 presents the PSD of both fresh and stored electrodes. Particle size ranges from ~7 μm to ~38 μm, with a  $d_{50}$  value of ~17 μm.

### 3.3. FTIR results

The FTIR measurements of both LFP and graphite electrodes are presented in Fig. 8. These measurements are performed on electrodes recovered from the fresh cell and cells stored at  $\text{SOC}_{\text{nom}} = 100\%$  and temperatures 30, 45, and 60 °C. The peaks seen for both spectra at 2364 cm<sup>-1</sup> and 2334 cm<sup>-1</sup> are typical of CO<sub>2</sub> in air and are not related to the electrodes. In Fig. 8(a), the spectrum of the fresh LFP electrode displays several peaks at 1140, 1045, and 950 cm<sup>-1</sup>. Those peaks around 1200–1000 cm<sup>-1</sup> can be attributed to P–O bond vibrations [22,23]. The spectra for aged electrodes present some disturbance in the region 1700–1300 cm<sup>-1</sup> corresponding to C=O bonds and a new peak at around 840 cm<sup>-1</sup>. Such a peak may reflect P–F bonds [24]. For the graphite electrode, we can see that the IR spectra are clearly influenced by the storage conditions (Fig. 8(b)). The spectra of aged electrodes display two peaks at 1645 cm<sup>-1</sup> and 1420 cm<sup>-1</sup>. It was mentioned earlier that the peaks in the 1700–1300 cm<sup>-1</sup> region reflect C=O bonds. A peak around 840 cm<sup>-1</sup> (P–F bonds) is also visible. Those peaks were

**Table 4**  
Residual and intrinsic capacities of the LiFePO<sub>4</sub> and graphite coin cells.

	LiFePO <sub>4</sub>			Graphite		
	Residual capacity (mAh cm <sup>-2</sup> )	Residual percentage <sup>a</sup>	Intrinsic capacity (mAh cm <sup>-2</sup> )	Residual capacity (mAh cm <sup>-2</sup> )	Residual percentage <sup>a</sup>	Intrinsic capacity (mAh cm <sup>-2</sup> )
Fresh	0.075	5.0	1.51 <sup>b</sup> /1.50 <sup>c</sup>	—	—	1.60 <sup>b</sup> /1.60 <sup>c</sup>
T30 SOC30	0.117	7.8	1.49 <sup>b</sup> /1.49 <sup>c</sup>	4.25 · 10 <sup>-3</sup>	0.26	1.63 <sup>b</sup> /1.63 <sup>c</sup>
T30 SOC65	0.096	6.5	1.47 <sup>b</sup> /1.46 <sup>c</sup>	3.60 · 10 <sup>-3</sup>	0.22	1.60 <sup>b</sup> /1.61 <sup>c</sup>
T30 SOC100	0.132	8.7	1.50 <sup>b</sup> /1.48 <sup>c</sup>	1.40 · 10 <sup>-3</sup>	0.09	1.62 <sup>b</sup> /1.63 <sup>c</sup>
T45 SOC30	0.157	10.3	1.52 <sup>b</sup> /1.51 <sup>c</sup>	2.25 · 10 <sup>-3</sup>	0.13	1.74 <sup>b</sup> /1.75 <sup>c</sup>
T45 SOC65	0.201	13.7	1.46 <sup>b</sup> /1.46 <sup>c</sup>	2.69 · 10 <sup>-3</sup>	0.17	1.58 <sup>b</sup> /1.59 <sup>c</sup>
T45 SOC100	0.192	12.8	1.50 <sup>b</sup> /1.49 <sup>c</sup>	2.03 · 10 <sup>-3</sup>	0.11	1.79 <sup>b</sup> /1.80 <sup>c</sup>
T60 SOC30	0.408	26.4	1.55 <sup>b</sup> /1.53 <sup>c</sup>	4.16 · 10 <sup>-8</sup>	0.25	1.68 <sup>b</sup> /1.69 <sup>c</sup>
T60 SOC65	0.413	28.1	1.47 <sup>b</sup> /1.45 <sup>c</sup>	5.71 · 10 <sup>-3</sup>	0.35	1.60 <sup>b</sup> /1.60 <sup>c</sup>
T60 SOC100	0.493	32.6	1.51 <sup>b</sup> /1.49 <sup>c</sup>	3.01 · 10 <sup>-3</sup>	0.19	1.62 <sup>b</sup> /1.63 <sup>c</sup>

<sup>a</sup> The residual percentage is calculated as (residual/intrinsic) × 100.

<sup>b</sup> The intrinsic capacity obtained from the last two cycles during charge.

<sup>c</sup> The intrinsic capacity obtained from the last two cycles during discharge.

barely seen for the fresh LFP and graphite electrode, thus suggesting that the electrodes develop rich surface chemistry upon storage.

### 3.4. Half-cell study

To understand better the capacity fade of the calendar-aged cells, half-cell studies (i.e., Li/LFP and Li/graphite cells) were performed on both fresh and aged electrodes. Residual and intrinsic (reversible) capacities were measured in both cases. For the positive LFP electrode, the residual capacity corresponds to the amount of empty sites left in the  $\text{FePO}_4$  framework when the full cell is fully discharged. As a consequence, during storage, the increase of residual capacity with the capacity fade of the full cell would be a strong indication for cyclable lithium loss because of side reactions, thus leading to a continuously less intercalated electrode at the end of discharge. For the graphite electrode, the residual capacity corresponds to the amount of lithium left in this electrode when the full cell is fully discharged. The intrinsic capacity, regardless of the electrode we consider, is related to the amount of active material in the electrode. The loss of active material in an electrode may result from different aging phenomena, e.g., metal dissolution for cathode materials and graphite particle isolation due to continuous SEI formation or graphite exfoliation at the anode.

#### 3.4.1. Formation cycles

The potential profiles of the four formation cycles of both fresh LFP and graphite electrodes are presented in Figs. 9 and 10, respectively. The inset associated with each figure shows a plot of charge and discharge capacities along with the corresponding coulombic efficiency as a function of cycle number. The formation

cycles for aged LFP and graphite electrodes are not displayed. The only difference between the formation cycles of fresh and aged electrodes is the initial discharge (i.e., lithium intercalation) of the LFP electrode and the initial charge (i.e., lithium deintercalation) of the graphite electrode. Those are used to calculate the residual capacities as mentioned in the Experimental section. The inset of Fig. 9 shows that, for the positive electrode, the charge capacity of first formation cycle is larger than that obtained during discharge, which suggests the occurrence of a side reaction (oxidation). The low value of coulombic efficiency ( $\sim 95\%$ ) at first cycle and its gradual increase upon further cycling ( $\sim 99.5\%$  at 4th cycle) might be related to the formation of a passive film at the surface of the electrode particles. For the negative electrode (inset of Fig. 10), the opposite is observed; the discharge capacity of the first formation cycle (i.e., during Li intercalation in graphite) is larger than the charge capacity. A side reaction (reduction) might be related to reformation/modification of the (already existing) SEI layer.

#### 3.4.2. Calendar data

The charge/discharge potential profiles of the 4th formation cycle are presented in Fig. 11(a) and (b) for the fresh LFP and graphite electrodes and for those from cells aged at  $\text{SOC}_{\text{nom}} = 100\%$  and at temperatures 30, 45, or 60 °C. Table 4 presents the residual and intrinsic capacities for all aged LFP electrodes. The various storage conditions do not lead to significant changes in the capacity values. The maximum capacity ( $1.55 \text{ mAh cm}^{-2}$ ) is measured during charge for an LFP electrode from a cell stored at 60 °C and  $\text{SOC}_{\text{nom}} = 30\%$ . The capacity is 2.5% larger than that of the fresh cell,

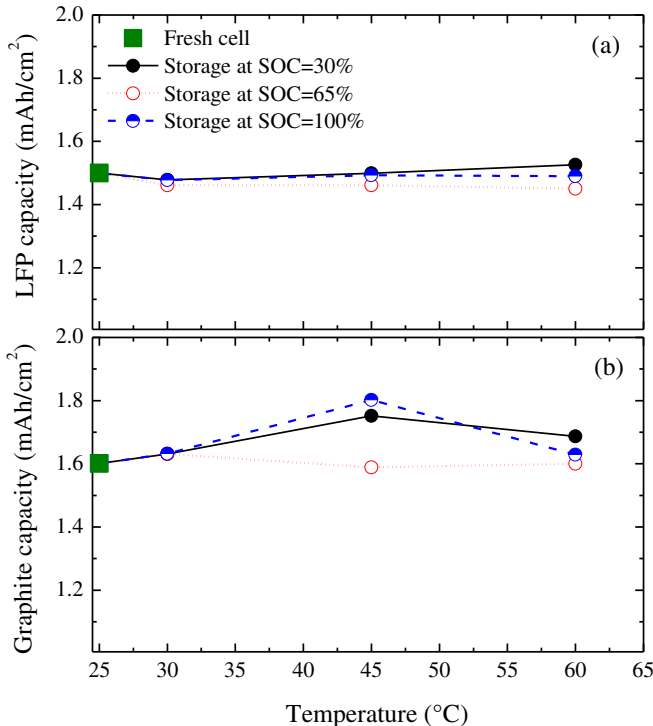


**Fig. 12.** Discharge capacities of the 4th formation cycle measured at  $C_{\text{nom}}/10$  and 25 °C of both (a) LFP and (b) graphite electrodes recovered from fresh cell and cells aged under different storage conditions of temperature and SOC.

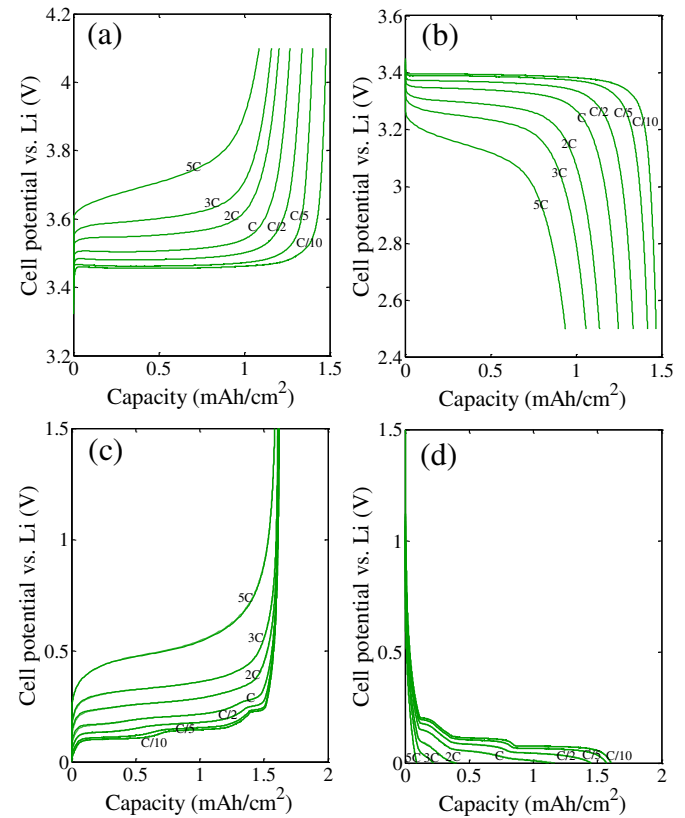


**Fig. 13.** Galvanostatic charge/discharge potential profiles measured at various C-rates and 25 °C for both (a, b) LFP and (c, d) graphite electrodes recovered from a fresh cell.

which probably results from cell-to-cell variations. Such an absence of capacity fade of LFP electrodes during storage (Fig. 12(a)) suggests that the electrode material does not undergo any structural degradation that causes capacity fade. Moreover, Table 4 shows that the maximum lithium content derived from the residual capacity ( $y$  in  $\text{Li}_y\text{FePO}_4$ ) gets lower with the severity of storage conditions. The initial composition of the cathode,  $\text{Li}_{0.95}\text{FePO}_4$  (fresh cell), becomes  $\text{Li}_{0.67}\text{FePO}_4$  (cell aged at 60 °C and  $\text{SOC}_{\text{nom}} = 100\%$ ). The LFP electrode becomes less intercalated at the end of discharge due to a loss of cyclable lithium.

Now moving to graphite, Fig. 11(b) shows that there is a 12% difference between the capacity of the fresh electrode and that from the cell aged at 45 °C and  $\text{SOC}_{\text{nom}} = 100\%$ , which probably results from some cell-to-cell variations due to the manufacturing process. Overall, the absence of intrinsic capacity fade (Fig. 12(b)) suggests that there is no degradation of the active material during storage. Table 4 also shows that the residual capacity of the graphite electrodes is negligible, which indicates that graphite electrodes are almost fully deintercalated during the discharge process applied to the full cells prior to being dismantled. The maximum stoichiometry of the graphite anode is found for the cell aged at 60 °C and  $\text{SOC}_{\text{nom}} = 65\%$  and corresponds to  $\text{Li}_{0.0035}\text{C}_6$ . This result is at odds with the bluish color of some graphite electrodes aged at 60 °C that would suggest the presence of residual lithium; we do not have any explanation for this apparent inconsistency.

### 3.4.3. Rate-capability tests

An example of charge/discharge potential profiles at various C-rates ranging from  $C_{\text{nom}}/10$  to  $5C_{\text{nom}}$  for both LFP and graphite electrodes recovered from a fresh cell is presented in Fig. 13(a,b) and (c,d), respectively. The corresponding rate-capability curves of fresh and aged LFP half-cells are provided in Fig. 14 and those of fresh and aged graphite half-cells are presented in Fig. 15. The LFP rate-capability curves show that the capacity decreases as the C-rate increases during both charge (Fig. 14(a–c)) and discharge (Fig. 14(d–f)). The curves also show that the delithiation process (charge) is more efficient than the lithiation one (discharge) for all the half-cells at high current density [25]. Aged LFP electrodes exhibit virtually no change in rate capability on both charge and discharge, which suggests negligible or minor increase of electrode resistance upon storage. This is also confirmed from EIS measurements presented in the next subsection. Fig. 15 shows that the graphite electrode performs much better during delithiation (Fig. 15(a–c)) than during lithiation (Fig. 15(d–f)). This is because the zero volt (0 V vs. Li) cutoff potential is very close to the potential range within which the graphite operates, on the contrary with the high cutoff value (1.5 V vs. Li). The rate-capability curves are pretty flat during charge except for the highest 5 C-rate, which seems to have a slight storage temperature and SOC dependence. During discharge, much significant changes appear around the 1 C-rate region. These are clear for the curves obtained from the cells aged at 45 °C and  $\text{SOC}_{\text{nom}} = 100\%$  and at 60 °C and  $\text{SOC}_{\text{nom}} = 30, 65$ , and

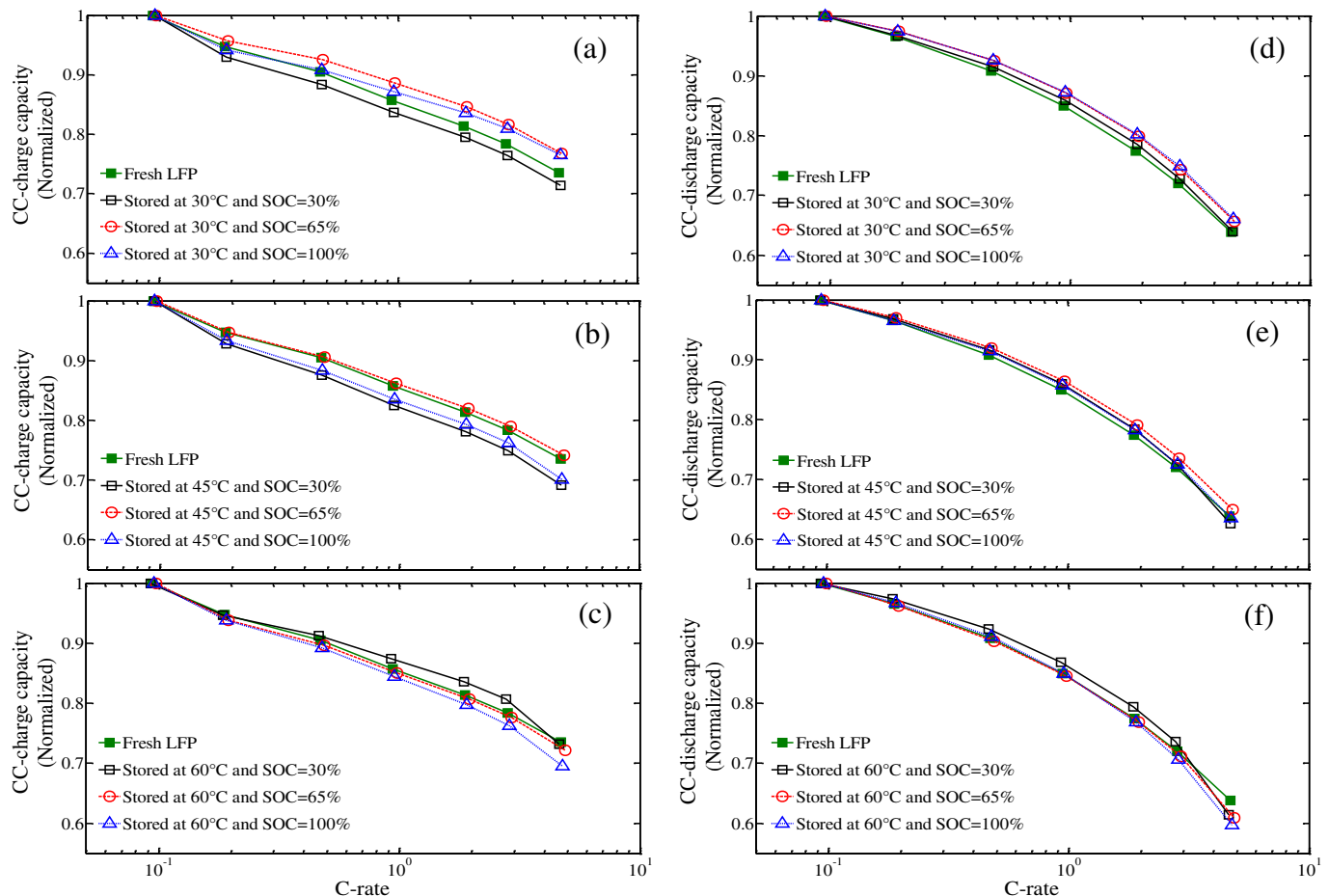


**Fig. 14.** Rate-capability plots of LFP recovered from both fresh and aged cells under different storage conditions of temperature and nominal SOCs, measured at 25 °C. (a–c) Rate capability on charge; (d–f) Rate capability on discharge.

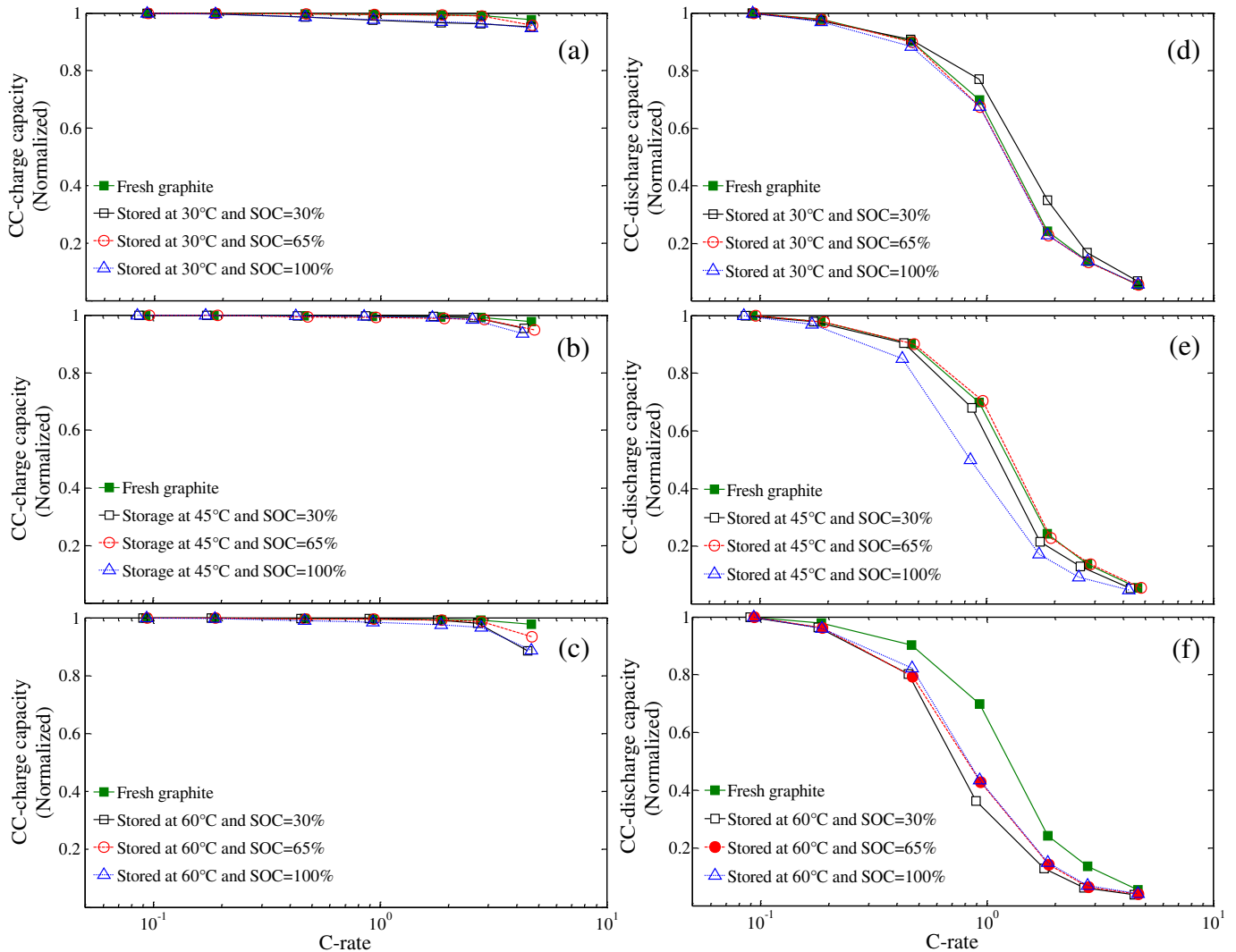


**Fig. 15.** Rate-capability plots of graphite recovered from both fresh and aged cells under different storage conditions of temperature and nominal SOCs, measured at 25 °C. (a–c) Rate capability on charge; (d–f) Rate capability on discharge.

100%. Such a change in the slope of rate-capability curves suggests a more significant change of the graphite impedance compared to that of LFP.

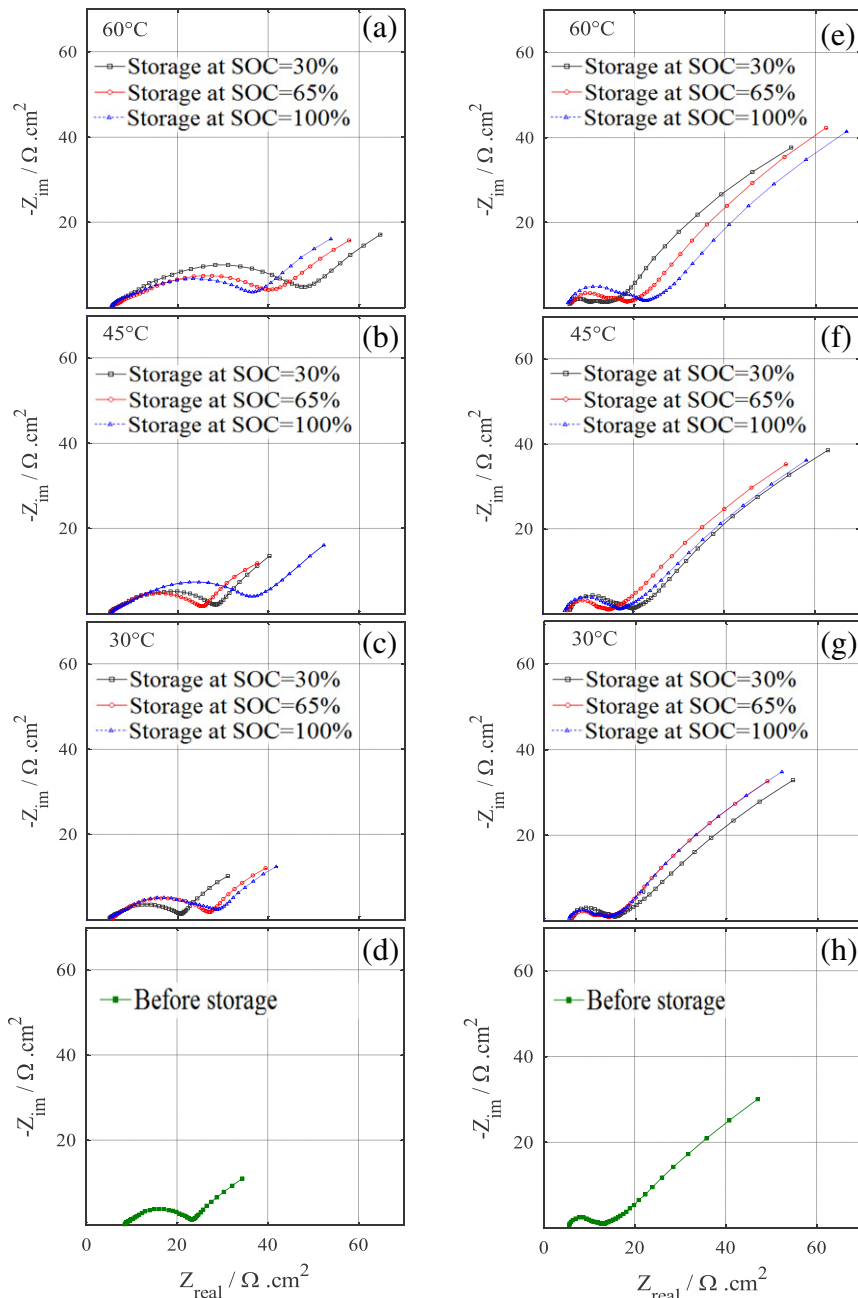
#### 3.4.4. Impedance test

Fig. 16 represents the Nyquist diagrams obtained for both graphite and LFP electrodes before and after storage at various temperatures and nominal SOCs. Fig. 16(a–d) shows that the impedance of the negative electrode increases with the storage temperature and that the effect of storage SOC is much less than that of the storage temperature. It is clearly seen that the highest impedance increase is for the electrodes stored at 60 °C. However, we observe a counterintuitive effect of the SOC at this temperature, i.e., the semi-circle part of the impedance related to interfacial phenomena is less at higher storage SOC. The evolution of the interfacial resistance values might be attributed to the reformation/modification of the SEI layer at the surface of the graphite particles, as evidenced from the SEM images (Fig. 6). Impedance measurements performed on the positive electrode are presented in Fig. 16(e–h). The semi-circle resistance becomes slightly larger upon storage. This minor evolution of the interfacial resistance is attributed to the small contribution of the resistive film formed at

the surface of electrode material. A direct evidence of formation of such a resistive surface film is the presence of the additional semi-circle in some spectra of aged LFP electrodes, in particular in those of electrodes aged at 60 °C.

#### 3.4.5. Stoichiometry window for LFP and graphite

Based on the above analysis of both LFP and graphite electrodes upon aging, it is interesting to understand whether one can predict the performance fade of the full cell based on changes of each electrode. To this end, the initial stoichiometries, the total superficial area, and the specific capacities of the two electrodes are required. First, the analysis of the recovered LFP electrodes by XRD and the analysis of residual discharge capacity of these same electrodes in coin cells showed a significant decrease in lithium stoichiometry of the LFP electrode due to aging (Fig. 17). An estimate of the stoichiometry of each LFP electrode was provided. The results of both methods (i.e., XRD or residual capacity) are fairly comparable. Such a result suggests that the loss of cyclable lithium is the main source of aging (coin-cell analyses on both LFP and graphite electrodes suggested no loss of active material due to electrode degradation). Secondly, the LFP and graphite electrode surface areas were measured after the cells were dismantled and



**Fig. 16.** Nyquist plots of the graphite (a–d) and LFP (e–h) electrodes recovered from both fresh and aged cells under different storage conditions of temperature and nominal SOC.

are  $0.72 \pm 0.01 \text{ m}^2$  and  $0.76 \pm 0.01 \text{ m}^2$ , respectively. The area of graphite electrode is  $\sim 4.6\%$  greater than that of the LFP electrode. This is consistent with other LiB cell designs reported in the literature and is useful to prevent lithium plating at the edges of the graphite electrode during charge [26,27]. Thirdly, the specific capacity of each electrode is directly measured with the coin cells. Then, a representation of battery internal balancing is constructed and presented in Fig. 18 [28,29]. Here, only the loss of cyclable lithium is considered, but the loss of active materials and increase in electrode polarization can be included if they are evidenced from coin-cell measurements. The stoichiometries of LFP electrodes in the discharged state allow for setting the relative position of the potential curves of each electrode. By positioning graphically the minimum (2 V) and maximum (3.65 V) cutoff

potentials, the full-cell capacity ( $Q_{\text{est}}$ ) and the stoichiometry of graphite at the end of charge ( $x^{\max}$ ) are determined.  $Q_{\text{est}}$  is generally higher than that obtained from PITT measurement on full cells ( $Q_{\text{exp}}$ ) [17]. The difference may come from several errors in the parameter estimates ( $y^{\max}$ ,  $Q_-$ ,  $Q_+$ , etc) or from possible composition nonuniformities within the battery. In Fig. 18, we have used  $Q_{\text{exp}}$  instead of  $Q_{\text{est}}$  in order to represent the battery internal balancing. This will provide access to new relative positions of the curves of each electrode and thus to new values of  $y^{\max}$  (green columns in Fig. 17). These  $y^{\max}$  values are generally lower than those obtained from XRD or coin-cell measurements. Although the  $y^{\max}$  values from the different methods differ from each other, they follow a similar variation as a function of storage conditions.

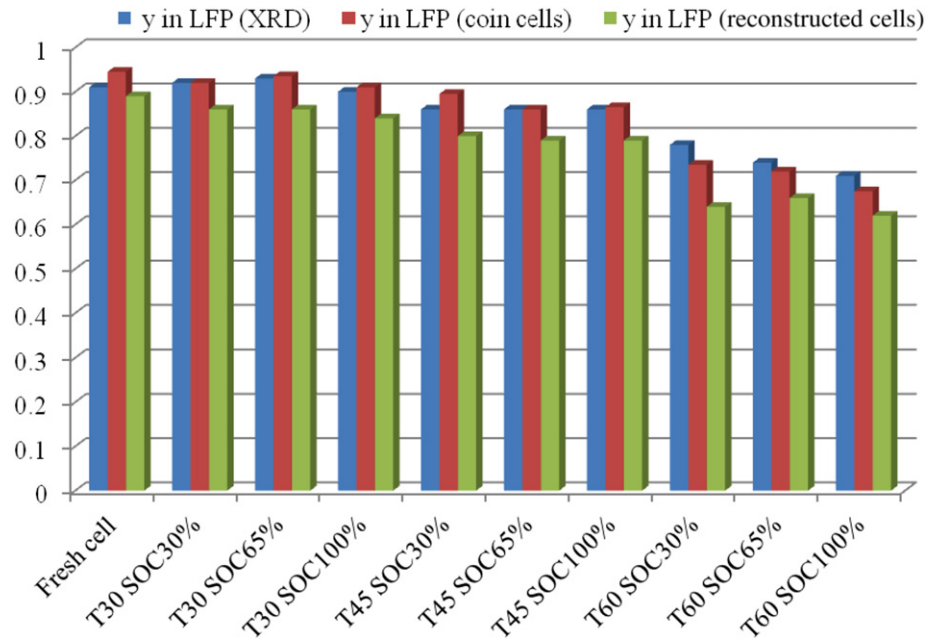


**Fig. 17.** Li stoichiometry obtained from (i) LFP/FP phase ratio from XRD patterns (blue columns), (ii) residual capacity of the Li/LFP coin cells assembled from the recovered positive electrodes (violet columns), and (iii) reconstructed cells (green columns). (For interpretation of the references to colour in this figure legend, the reader is referred to the web version of this article.)

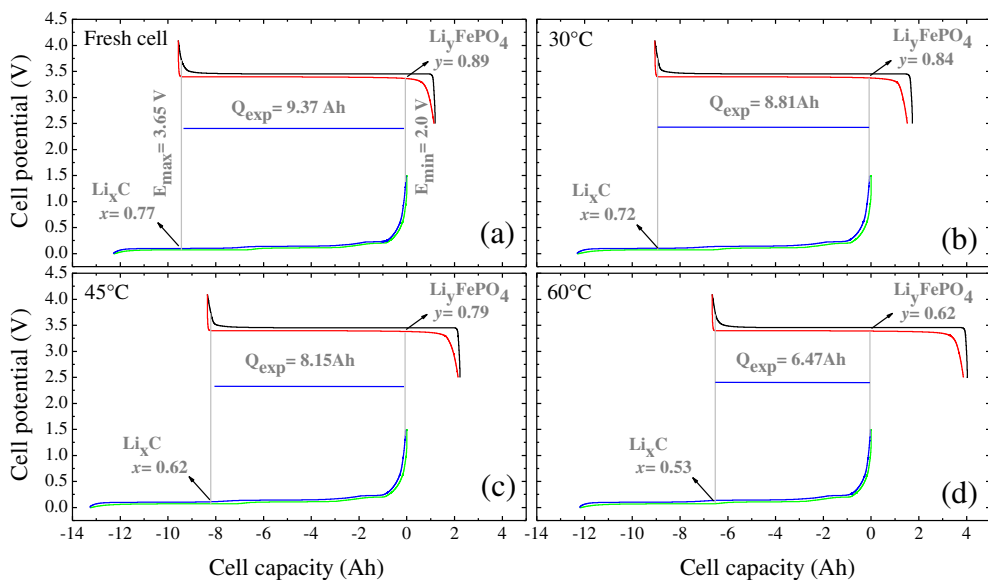


**Fig. 18.** Operating stoichiometry window of the graphite/LFP cell. (a) Fresh cell, (b) cell aged at 30 °C and  $\text{SOC}_{\text{nom}} = 100\%$ , (c) cell aged at 45 °C and  $\text{SOC}_{\text{nom}} = 100\%$ , and (d) cell aged at 60 °C and  $\text{SOC}_{\text{nom}} = 100\%$ .

#### 4. Conclusion

This study presents the postmortem analysis of commercial graphite/LiFePO<sub>4</sub> cells aged under storage in different conditions of temperature (30 °C, 45 °C, and 60 °C) and nominal state of charge (30%, 65%, and 100%). The cells were disassembled under inert atmosphere in their discharged state, and XRD, SEM, FTIR, and half-cell studies were carried out. XRD results indicate no structural change of both LFP and graphite materials upon storage. An analysis of the XRD patterns of the positive electrodes also shows that the overall lithium stoichiometry of the LFP electrode ( $y$  in Li<sub>y</sub>FePO<sub>4</sub>) decreases with the severity of storage condition (the storage

condition with the highest temperature and SOC is the most severe). SEM shows that, for the LFP electrode, aging leads to the appearance of F-rich round-shape particles at storage temperatures of 45 and 60 °C, the size of which is related to the storage temperature. For the graphite electrode, aging leads to the appearance of a thick and fluffy SEI at the graphite particle surface, especially for the electrode stored under the most severe conditions (e.g.,  $T = 60$  °C and  $\text{SOC}_{\text{nom}} = 100\%$ ). It is also reflected in the O content from EDS analysis that increases with the severity of the aging conditions. FTIR results imply that both electrodes develop rich surface chemistry upon storage. Intrinsic capacity tests of both LFP and graphite electrodes rule out the structural degradation of the

electrode material as a cause of capacity fade. Residual capacities of LFP electrodes show that the maximum lithium content ( $y^{\max}$ ) gets lower with the severity of storage conditions. On the other hand, the negligible residual capacity of the graphite electrodes indicates that they are almost fully deintercalated during the discharge process applied to the full cells prior to being dismantled. Rate-capability tests suggest a negligible or minor increase of LFP electrode resistance upon storage and a more significant change of the graphite impedance. EIS analysis confirms this suggestion and the change of the graphite impedance is more significant compared with that of LFP.

Overall, the results show that (i) the loss of cyclable lithium is the main source of aging (XRD and residual capacity measurements show that the maximum lithium stoichiometry ( $y^{\max}$ ) of the LFP electrode recovered from the full cell at a fully discharged state, comparable for both techniques, gets lower with the severity of storage conditions), and (ii) there is no loss of active material (capacity measurements on separate electrodes show that there is no fade upon storage).

## Acknowledgments

This work was funded by the French National Research Agency (ANR) under the SIMCAL research program. The authors would like to acknowledge J. N. Chotard (LRCS) and K. Djellab (Microscopy platform of UPJV) for useful discussion on XRD and SEM/EDS techniques, respectively. The authors also acknowledge S. Laruelle and S. Grugueon (LRCS) for their help with FTIR.

SIMCAL network partners: **CEA**: B. Crouzevialle, A. Delaille, S. Grolleau, S. Mailley, B. Molina-Concha, **EDF**: L. Jamy, **EIGSI**: F. Duclaud, A. Mieze, A. Guignard, **IFP Energies Nouvelles**: J. Bernard, R. Revel, F. Moreau, I. Clémenton, D. Audigier, F. Badin, **IFSTTAR**: S. Pélassier, J. Peter, **IMS**: J.M. Vinassa, O. Briat, A. Eddahech, H. Henry, **LEC**: C. Forgez, G. Friedrich, **LMS-Imagine**: J. Hafsaoui, P. Aubret, **LRCS**: M. Morcrette, C. Delacourt, M. Kassem, **MTA Platform**: C. Adès, **PSA Peugeot Citroën**: D. Porcellato, M. Capelle, T. Prenant, S.

Joly, **RENAULT**: P. Gyan, **SAFT**: S. Bourlot, **VALEO**: M. Ouattara-Brigaudet, D. Benchetrite.

## References

- [1] K. Ozawa, Solid State Ionics 69 (1994) 212.
- [2] A.K. Padhi, K.S. Nanjundaswamy, J.B. Goodenough, J. Electrochem. Soc. 144 (1997) 1188.
- [3] A.K. Padhi, K.S. Nanjundaswamy, C. Masquelier, S. Okada, J.B. Goodenough, J. Electrochem. Soc. 144 (1997) 1609.
- [4] K. Striebel, A. Guerfi, J. Shim, M. Armand, M. Gauthier, K. Zaghib, J. Power Sources 119–121 (2003) 951.
- [5] J. Shim, K.A. Striebel, J. Power Sources 119–121 (2003) 955.
- [6] K. Zaghib, K. Striebel, A. Guerfi, J. Shim, M. Armand, M. Gauthier, Electrochim. Acta 50 (2–3) (2004) 263.
- [7] M. Dubarry, B.Y. Liaw, J. Power Sources 194 (1) (2009) 541.
- [8] K. Amine, J. Liu, I. Belharouak, Electrochim. Commun. 7 (2005) 669.
- [9] M. Koltypin, D. Aurbach, L. Nazar, B. Ellis, Electrochim. Solid State Lett. 10 (2) (2007) A40.
- [10] M. Koltypin, D. Aurbach, L. Nazar, B. Ellis, J. Power Sources 174 (2) (2007) 1241.
- [11] P. Liu, J. Wang, J. Hicks-Garner, E. Sherman, S. Soukiazian, M. Verbrugge, H. Tataria, J. Musser, P. Finamore, J. Electrochem. Soc. 157 (2010) A499.
- [12] J. Wang, P. Liu, J. Hicks-Garner, E. Sherman, S. Soukiazian, M. Verbrugge, H. Tataria, J. Musser, P. Finamore, J. Power Sources 196 (2011) 3942.
- [13] M. Dubarry, B.Y. Liaw, Mao-Sung Chen, S.S. Chyan, K.C. Han, W.T. Sie, S.H. Wu, J. Power Sources 196 (2011) 3420.
- [14] S.B. Peterson, J. Apt, J.F. Whitacre, J. Power Sources 195 (2010) 2385.
- [15] M. Safari, C. Delacourt, J. Electrochem. Soc. 158 (10) (2011) A1123.
- [16] M. Safari, C. Delacourt, J. Electrochem. Soc. 158 (12) (2011) A1436.
- [17] M. Kassem, J. Bernard, R. Revel, S. Pelissier, F. Duclaud, C. Delacourt, J. Power Sources 208 (2012) 296.
- [18] <http://www.lifebatt.co.uk>.
- [19] Y. Ozawa, R. Yazami, B. Fultz, J. Power Sources 119–121 (2003) 918.
- [20] C. Delacourt, Ph.D. thesis, Université de Picardie Jules Verne (2005).
- [21] P. Maire, H. Kaiser, W. Scheifele, P. Novák, J. Electroanal. Chem. 644 (2010) 127.
- [22] X.H. Guan, C. Shang, J. Zhu, G.H. Chen, J. Colloid Interface Sci. 293 (2006) 296.
- [23] M. Koltypin, D. Aurbach, L. Nazar, B. Ellis, Electrochim. Solid State Lett. 10 (2) (2007) A40–A44.
- [24] D. Aurbach, M. Moshkovich, Y. Cohen, A. Schechter, Langmuir 15 (1999) 2947.
- [25] M. Farkhondeh, C. Delacourt, J. Electrochem. Soc. 159 (2012) A177.
- [26] K. Kumaresan, Q. Guo, P. Ramadass, R.E. White, J. Power Sources 158 (1) (2006) 679.
- [27] M. Tang, P. Albertus, J. Newman, J. Electrochem. Soc. 156 (5) (2009) A390.
- [28] C. Delacourt, M. Safari, J. Electrochem. Soc. 159 (8) (2012) A1283.
- [29] M. Dubarry, C. Truchot, B.Y. Liaw, J. Power Sources 219 (2012) 204.